

Study on the Probability Distribution of Pitting for Naturally Corroded Prestressing Strands Accounting for Surface Defects

*Original*

Study on the Probability Distribution of Pitting for Naturally Corroded Prestressing Strands Accounting for Surface Defects / Franceschini, Lorenzo; Belletti, BEATRICE CARLA; Tondolo, Francesco; Sanchez, Javier. - In: BUILDINGS. - ISSN 2075-5309. - 12:10(2022), p. 1732. [10.3390/buildings12101732]

*Availability:*

This version is available at: 11583/2973334 since: 2022-11-23T16:58:47Z

*Publisher:*

MDPI

*Published*

DOI:10.3390/buildings12101732

*Terms of use:*

This article is made available under terms and conditions as specified in the corresponding bibliographic description in the repository

*Publisher copyright*

(Article begins on next page)

## Article

# Study on the Probability Distribution of Pitting for Naturally Corroded Prestressing Strands Accounting for Surface Defects

Lorenzo Franceschini <sup>1,\*</sup> , Beatrice Belletti <sup>1</sup>, Francesco Tondolo <sup>2</sup>  and Javier Sanchez <sup>3</sup> 

<sup>1</sup> Department of Engineering and Architecture, University of Parma, Parco Area delle Scienze 181/A, 43124 Parma, Italy

<sup>2</sup> Department of Structural, Geotechnical and Building Engineering, Politecnico di Torino, Corso Duca degli Abruzzi 24, 10129 Turin, Italy

<sup>3</sup> Institute Eduardo Torroja of Construction Sciences, Serrano Galvache, 28033 Madrid, Spain

\* Correspondence: lorenzo.franceschini@unipr.it

**Abstract:** One of the most urgent scientific needs from a technical and economic engineering point of view is the assessment of concrete structures suffering corrosion deterioration. However, the pursuit of this target in the case of corroded prestressed concrete (PC) members is hindered by the lack of (i) consolidated simplified formulations to be used in the engineering daily practice and (ii) works investigating the uncertainties in the correlation between the damage induced by corrosion and the structural resistance. To this aim, the present study adopts a 3D-scanning technique for the pitting morphology evaluation of several corroded prestressing strands retrieved from 10-year-old PC beams. First, the probabilistic distributions of penetration depths have been investigated. Second, the pitting factors  $\alpha$  and  $\Omega_i$  have been proposed and discussed to quantify the level of corrosion in longitudinal and transversal direction, respectively. Finally, correlations have been derived between the maximum and average penetration depth as a function of the level of corrosion and the surface defects mapping has been carried out on the corroded PC beams. The results show that the penetration depth of strands subjected to chloride-induced corrosion can be best fitted by a lognormal distribution function. Additionally, the simultaneous consideration of longitudinal and transversal pitting factor is found out to be essential for an exhaustive comprehension of pitting corrosion. Moreover, the outcomes highlight that the presence of longitudinal splitting cracks plays a fundamental role in the corrosion spatial variability of prestressing strands.

**Keywords:** corrosion-induced cracks; natural corrosion; pitting; prestressing steel; probability distribution; statistical analysis; 3D scanning



**Citation:** Franceschini, L.; Belletti, B.; Tondolo, F.; Sanchez, J. Study on the Probability Distribution of Pitting for Naturally Corroded Prestressing Strands Accounting for Surface Defects. *Buildings* **2022**, *12*, 1732. <https://doi.org/10.3390/buildings12101732>

Academic Editor: Nikolai Ivanovich Vatin

Received: 16 August 2022

Accepted: 17 October 2022

Published: 19 October 2022

**Publisher's Note:** MDPI stays neutral with regard to jurisdictional claims in published maps and institutional affiliations.



**Copyright:** © 2022 by the authors. Licensee MDPI, Basel, Switzerland. This article is an open access article distributed under the terms and conditions of the Creative Commons Attribution (CC BY) license (<https://creativecommons.org/licenses/by/4.0/>).

## 1. Introduction

As is widely known, concrete is the world's most-used man-made material [1]. Thanks to the use of this material, a variety of reinforced (RC) and prestressed (PC) concrete structures and infrastructures are built daily: buildings, bridges, power and nuclear plants, tunnels, etc. Although these facilities play an important role in ensuring the regular course of everyone's daily life, from an economic point of view they can require high costs for maintenance if not properly designed against corrosion attack [2–4] or seismic actions [5]. In fact, the aggressiveness of the exposure environment, the intensive use of de-icing salt during cold periods or climate changes related to increased CO<sub>2</sub> emissions lead to substantial durability issues that limit the service life of RC and PC structures and infrastructures over time [6,7].

Currently, reinforcement corrosion is considered as the main cause in the reduction in the performance and durability of concrete structures [8–10]. Therefore, the assessment of deteriorating structures is addressed as one of the most urgent scientific needs from a technical and economic engineering point of view. Since the consequences of corrosion in PC elements could be more serious than in RC ones because of the combination of

high mechanical stresses applied to prestressing strands and the cross-section loss of reinforcements that enhances the risk of brittle failure, the chloride-induced corrosion deterioration in PC structures should be carefully investigated [11,12].

Even if several efforts have been devoted to the assessment of the residual response and behavior of PC members affected by corrosion deterioration [13–17], the topic still needs further study. In particular, no clear guidelines on the assessment of the deterioration state and the corresponding strength of these existing structures are available; consequently, the engineering daily practice is limited by the lack in scientific literature of well-consolidated, simplified formulations and studies that investigate the uncertainties in the correlation between the damage induced by corrosion and the structural resistance.

To fill the lack, the present study investigates six 10-year-old PC beams subjected to chloride-induced corrosion by mapping their surface defects before failure testing and by adopting a 3D-scanning technique for the pitting morphology evaluation of several corroded prestressing strands. Thereafter, based on the outcomes from the sectional analysis conducted on the available corroded samples, the best probabilistic distribution function for the description of the penetration depth is first determined by comparing normal, lognormal and Gumbel extreme-value distributions. Second, the variation of longitudinal and transversal pitting factors is analyzed. In particular, a new correlation for the prediction of the sectional average penetration depth of external wires  $P_{pit,av,sectional,i}$  is proposed, starting from the single measurement of the maximum penetration depth in the same section  $P_{pit,max,i}$ . Finally, while investigating the influence of longitudinal splitting cracks on pitting corrosion of prestressing strands, a new measurement-based correlation that relates the maximum  $P_{pit,max}$  and the longitudinal average penetration depths  $P_{pit,av,long}$  of corroded prestressing strands is defined.

To conclude, the obtained statistical distributions as a function of the different levels of corrosion can be used as a starting point for more refined probabilistic simulations, such as Monte Carlo analyses [18], with the aim of pursuing a detailed description of the evolution of the chloride-induced corrosion over time. On the other hand, the simplified approach for the estimation of the sectional average penetration depth of external wires  $P_{pit,av,sectional,i}$  can be a useful parameter for the prediction of the tensile resistance decay of corroded prestressing strands by adopting the equivalent spring model [19,20]. Finally, although the proposed correlation between surface defects and the reinforcements' level of corrosion should be further validated and improved, the obtained results contribute to finding the key parameters and to preliminarily distinguish the behavior of cracked and uncracked PC members.

## 2. Materials and Methods

### 2.1. Specimens Description

The PC beams came from a refrigeration tower of a Spanish thermal power plant, where they were subjected to an aggressive environment for 10 years. The beams were part of a wide experimental campaign carried out on 11 naturally corroded PC beams at the Instituto Eduardo Torroja of Madrid, where 3-point and 4-point bending tests were carried out to analyze their residual flexural and shear capacity as a function of the detected variable level of corrosion [21,22].

The present study involves six out eleven 5210 mm long pre-tensioned prestressed concrete beams, named PB9-PB10-PB11-PB12-PB13 and PB14, with cross-sectional dimensions equal to  $150 \times 300 \text{ mm}^2$ . Each beam was characterized by two  $\phi 5$  ribbed bars as top longitudinal reinforcement and two 12.9 mm seven-wire prestressing strands with an eccentricity of 100 mm as bottom reinforcement. For the single prestressing strand not impaired by the presence of corrosion, the six external wires and the inner one had a radius equal to 2.13 mm ( $r_{outer}$ ) and 2.19 mm ( $r_{inner}$ ), respectively, leading to an overall uncorroded cross-sectional area of the strand equal to  $100 \text{ mm}^2$ . The thickness of the concrete cover was equal to 45 and 50 mm for top and bottom reinforcement, respectively, whereas no transver-

sal reinforcements were provided. The beams' geometrical features are summarized in Figure 1.

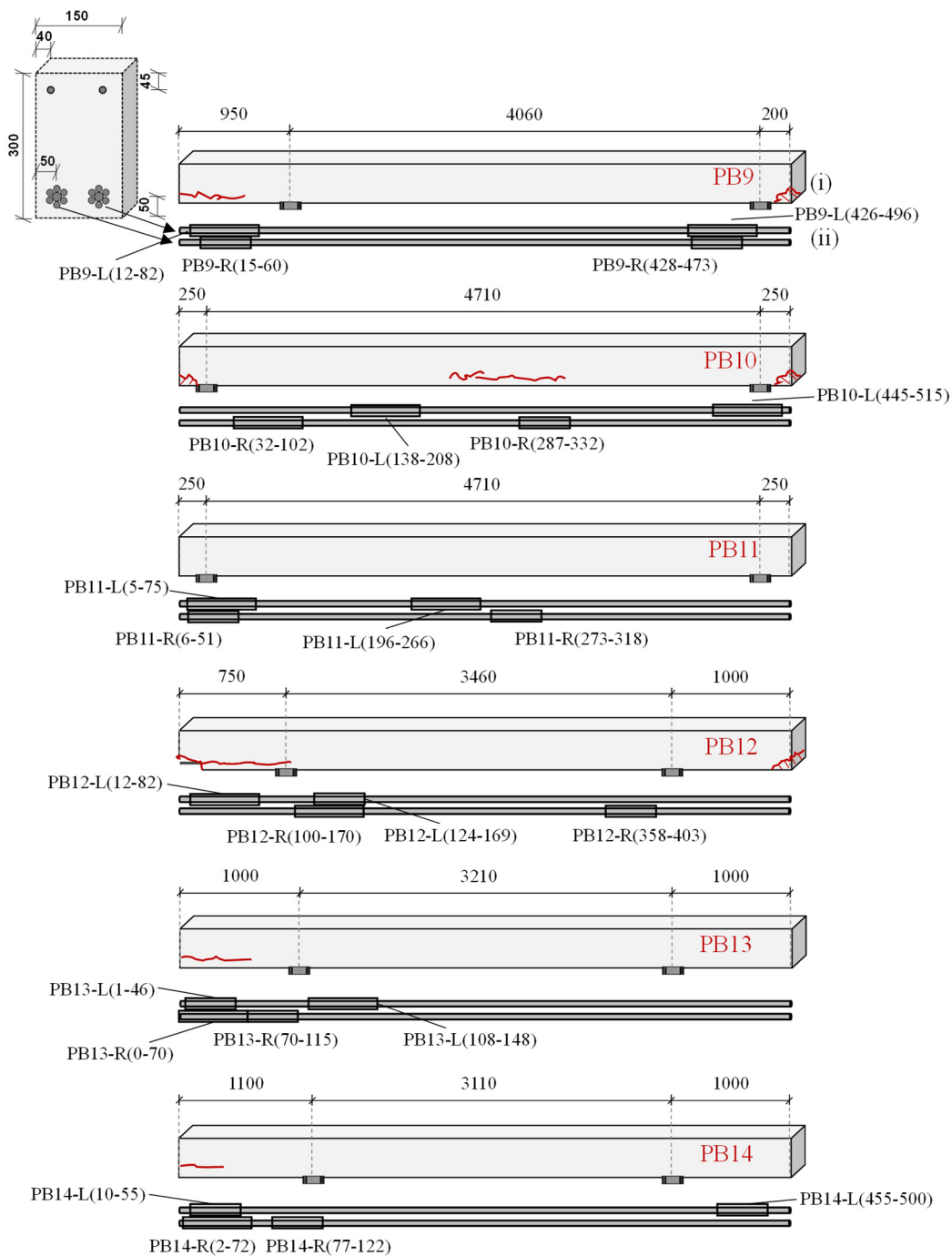


**Figure 1.** Features of corroded PC beams: (i) identification of corrosion-induced longitudinal splitting cracks, (ii) samples' locations.

## 2.2. Mapping of Longitudinal Cracks

During the characterization of the available specimens, a design deficiency was identified as the main cause of corrosion. Indeed, no strand protection was provided at the edges of the beams, leaving the prestressing strands free to corrode. Therefore, a significant chloride-induced corrosion occurred in 10 years of service, especially at beam-end sides because of the cooling wet–dry cycles carried out by using seawater.

Before testing, corrosion-induced longitudinal splitting cracks caused by the formation of rust products and the subsequent increase in pressure at the interface between concrete and prestressing steel were observed at one or both end sides of all the investigated beams, except for beams PB10 and PB11. In detail, PB10 showed longitudinal splitting cracks at the mid-span region, whereas PB11 was characterized by no surface defects. For the sake of clarity, Figure 1i reports the location of the longitudinal splitting cracks for each investigated PC beam. It is worth noting that the crack opening was not measured. After testing, the corroded prestressing strands were extracted from each beam and a qualitative visual inspection was performed to determine the variation of the level of corrosion along their overall length.

Thereafter, a total of 24 prestressing strand samples—four for each beam—were retrieved at different locations, as reported in Figure 1ii [16,23]. To classify the available samples, an identifying code has been adopted in the form PBx-L(yy-zz) or PBx-R(yy-zz), where PB stands for prestressed beam, x is a number ranging from 9 to 14 and identifies the reference beam the sample came from, the letter L or R details the left or right side position, respectively, of the prestressing strand in the cross-section and the coordinates in brackets yy-zz stand for the initial and final abscissa (measured from the left-hand-side edge of the beam) at which the sample was retrieved. First, the samples were classified according to their length by distinguishing 12 samples 450 mm long and 12 samples 750 mm long. Then, the second classification was performed by subdividing the samples retrieved or not from beam zones characterized by the presence of former surface defects, named “cracked” and “uncracked”, aiming to analyze the influence of longitudinal splitting cracks induced by corrosion, as reported in Table 1. Since four samples—PB9-R(428-473), PB11-L(5-75), PB12-R(358-403) and PB14-L(455-500)—showed no corrosion signs during the visual inspection, they were assumed to be uncorroded reference samples (Table 1).

### 2.3. Corrosion Data Measurement

To accurately investigate the effects of corrosion, geometrical parameters such as the residual cross-sectional area, the number of pits, their spatial variability and penetration depth along the sample length were measured using a 3D-scanning technique. This latter methodology is generally recognized by the scientific community as the more precise technique for the evaluation of the geometrical parameters of pitting corrosion since it avoids the shortcomings of other types of techniques, such as weight loss, vernier caliper or drainage methods [24,25]. The present research will focus on pit-depth analysis, while other geometrical parameters have been covered in prior works [16,23].

Figure 2 shows the 3D-scanning set-up, which was composed by:

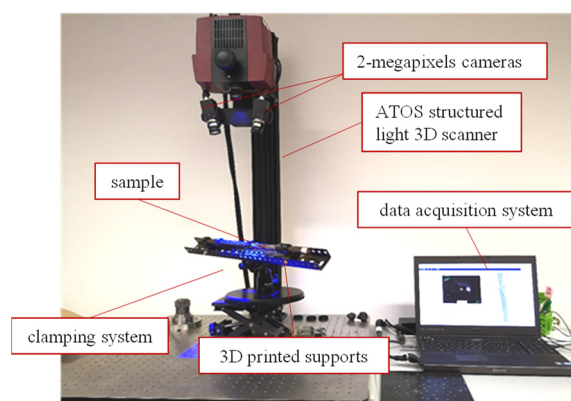
- Clamping system: a metal support plate and two 3D-printed bearings of ABS material, which allow to fix samples with variable length and to rotate them along the longitudinal axis during the scanning procedure.
- 3D-printed supports that were realized by using PLA filament.
- ATOS Compact structured-light 3D scanner with two 2-megapixel cameras that allow the application of the triangulation principle to measure the 3D coordinates of points on the sample surface.
- Data acquisition system: an STL format was used to export the virtual model of the sample geometry, which consisted of tessellated surfaces using triangles constructed from a cloud of points scattered in space resulting from 3D-scanning activity.

It is worth noting that the scanned length of each sample was reduced by 100 mm on both sides and resulted in them being equal to 250 mm and 500 mm for samples belonging to the groups 450 mm and 750 mm long, respectively, to consider the presence of the gripping system during the following tensile tests [26].

**Table 1.** Characterization of pitting corrosion of retrieved corroded prestressing strands.

Identifying Code	Surface Defects (Splitting Cracks)	$P_{pit,max}/r_{outer}$ [-]	$P_{pit,av,long}/r_{outer}$ [-]	$\eta$ [%]
PB9-L(12-82)	v	0.80	0.29	17.30
PB9-L(426-496)	x	0.20	0.02	2.80
PB9-R(15-60)	v	1.31	0.33	21.50
PB9-R(428-473)	Uncorroded	-	-	-
PB10-L(138-208)	x	0.28	0.03	2.40
PB10-L(445-515) * <sup>1</sup>	x	1.20	0.20	6.30
PB10-R(287-332) * <sup>1</sup>	v	1.35	0.24	8.00
PB10-R(32-102) * <sup>2</sup>	-	-	-	-
PB11-L(5-75)	Uncorroded	-	-	-
PB11-L(196-266)	x	0.66	0.10	2.90
PB11-R(6-51)	x	0.46	0.06	2.00
PB11-R(273-318)	x	0.59	0.11	4.80
PB12-L(12-82)	v	0.73	0.25	14.20
PB12-L(124-169)	x	0.58	0.14	4.30
PB12-R(100-170)	x	0.47	0.15	5.30
PB12-R(358-403)	Uncorroded	-	-	-
PB13-L(1-46)	v	0.69	0.20	7.60
PB13-R(0-70)	v	0.65	0.23	11.40
PB13-L(108-178) * <sup>1</sup>	x	0.86	0.28	4.30
PB13-R(70-115)	x	0.47	0.14	4.60
PB14-L(455-500)	Uncorroded	-	-	-
PB14-L(10-55)	v	1.05	0.31	14.70
PB14-R(2-72)	v	0.58	0.23	11.60
PB14-R(77-122)	x	0.25	0.08	3.80

\*<sup>1</sup> Samples not considered in the following relationship because of outliers. \*<sup>2</sup> Samples not considered because of 3D-scanning problems.

**Figure 2.** 3D-scanning activity set-up.

Thereafter, the virtual model (STL format) was uploaded within the GOM Inspect software for the repairing phase that consists of filling in small holes and of the removal of noise points. Then, by adopting the principle of superimposition, the 3D models of the uncorroded reference sample and the corroded sample—in the form of repaired mesh—were compared to measure the variation of geometrical parameters along the overall sample length. In detail, the superimposition phase was ensured by the use of the best-fit algorithm implemented in GOM Inspect software, which iteratively computes the roto-translation matrix to be applied to the compared data for minimization of the alignment and superposition error with respect to the reference data.

Finally, the experimental procedure adopted by Li et al. [24] for the evaluation of the geometrical parameters of corroded steel bars was applied for the measurement of the pitting parameters, such as the penetration depth of pits in the external wires,  $P_{pit,i}$ . In

detail, the analysis was carried out sectionally at a spacing of 10 mm along the length of each corroded prestressing strand sample, as highlighted in Figure 3.

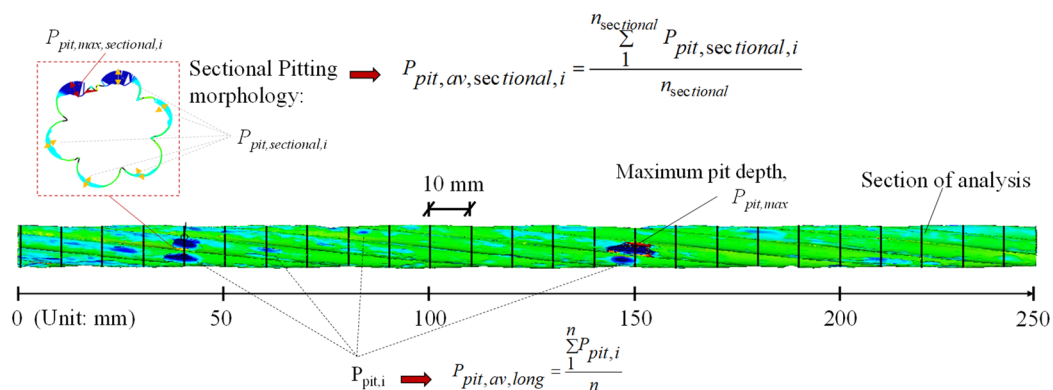


**Figure 3.** Example of 3D-model superimposition for the measurement of geometrical pitting parameters in the case of 250 mm long scanned length: (i) with a focus on sectional analysis every 10 mm and (ii) definition of the main pitting parameters.

In this framework, the following relevant geometrical parameters have been defined:

- ❖  $P_{pit,max}$ , which corresponds to the maximum penetration depth measured along the overall length of each corroded sample, as in Figure 3.
- ❖  $P_{pit,av,long}$ , which corresponds to the longitudinal average penetration depth of each corroded sample—calculated as the mathematical average of penetration depths of scanned pits,  $P_{pit,i}$ , measured along the overall length of each sample, as expressed in Equation (1):

$$P_{pit,av,long} = \frac{\sum_{1}^n P_{pit,i}}{n} \quad (1)$$

where  $n$  stands for the total number of scanned pits,  $P_{pit,i}$ .

- ❖  $P_{pit,max,sectional,i}$ , which corresponds to the sectional maximum penetration depth measured sectionally every 10 mm along the length of each sample.
- ❖  $P_{pit,av,sectional,i}$ , which corresponds to the sectional average penetration depth of each corroded sample—calculated as the mathematical average of penetration depths measured sectionally,  $P_{pit,sectional,i}$ , except for the most corroded one,  $P_{pit,max,sectional,i}$ , through the expression reported in Equation (2):

$$P_{pit,av,sectional,i} = \frac{\sum_{1}^{n_{sectional}} P_{pit,sectional,i}}{n_{sectional}} \quad (2)$$

where  $n_{sectional}$  is set equal to 5 and stands for the number of external wires minus the most corroded where  $P_{pit,max,sectional,i}$  is measured.

Additionally, the mass loss  $\eta$  (%) was measured for each sample by conducting the gravimetric method specified by the ASTM G1-03 standard [27], as expressed in Equation (3):

$$\eta = \frac{m_0 - m_{corr}}{m_0} \cdot 100 \quad (3)$$

where  $m_0$  and  $m_{corr}$  are the weight of the uncorroded and corroded reinforcement samples, respectively. For each sample, Table 1 reports the mass loss  $\eta$  and the dimensionless values of the geometrical parameters obtained by dividing the quantities  $P_{pit,max}$  and  $P_{pit,av,long}$  by the uncorroded value of the radius of external wires,  $r_{outer}$ ; the variability of the dimensionless value  $P_{pit,av,sectional,i}$  is discussed in Section 3.2.3.

### 3. Results and Discussion

The present contribution identifies the maximum and average penetration depths measured in longitudinal and transversal directions as the crucial geometrical features for a detailed description of the behavior of prestressing reinforcement subjected to chloride-induced corrosion. On the other hand, several studies available in the scientific literature selected the mass loss  $\eta$  measurement as the main parameter for the prediction of the residual behavior of corroded reinforcements or prestressing strands, such as the investigation of the decay of mechanical properties [28–30]. To maximize the usefulness of the obtained results, the first step involves the definition of new relationships that correlates the mass-loss measurements with the penetration-depth values, as highlighted in Figure 4. In detail, the dashed red and grey lines, the expressions of which are reported in Equations (4) and (5), show the experimental relations between the overall maximum penetration depth,  $P_{pit,max}$ , or the longitudinal average penetration depth,  $P_{pit,av,long}$ , with respect to the mass loss  $\eta$  of each corroded sample.

$$\frac{P_{pit,max}}{r_{outer}} = 0.0626\eta \quad (4)$$

$$\frac{P_{pit,av,long}}{r_{outer}} = 0.0186\eta \quad (5)$$

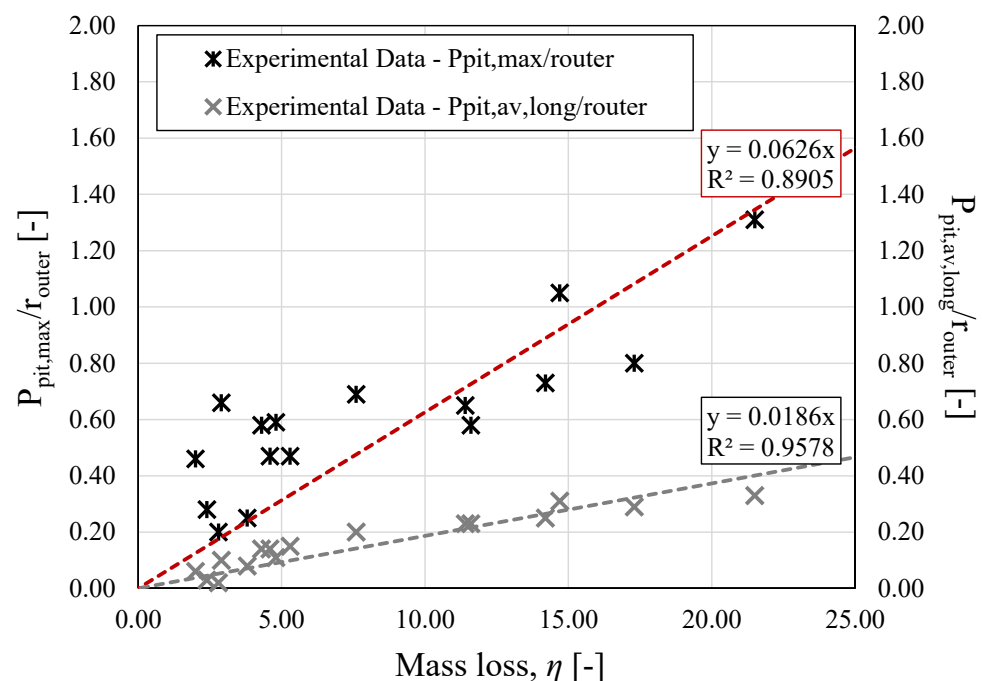


**Figure 4.** Relationships of  $P_{pit,max}/r_{outer}$  and  $P_{pit,av,long}/r_{outer}$  versus mass loss  $\eta$ .

Based on the obtained outcomes, a significant correlation between the analyzed data is observed, as confirmed by the coefficients of correlation  $R^2$  equal to 0.89 and 0.96 obtained in the case of  $P_{pit,max}$  and  $P_{pit,av,long}$ , respectively. As a matter of fact, the  $P_{pit,max}$ - $\eta$  correlation is affected by a greater dispersion of results if compared to the  $P_{pit,av,long}$ - $\eta$  relation.

#### 3.1. Analysis of the Probabilistic Distributions of Penetration Depth

In this section, the probability distribution functions of penetration depth for each corroded prestressing strands are studied. As the first step, the pit depths of each external wire of the strands were measured by adopting the sectional analysis highlighted in Figure 3 and previously described in paragraph 2.2. Then, normal, lognormal, and Gumbel extreme-value distributions have been fitted to the measured experimental data with the aim to establish the best probabilistic distribution function. Figure 5 reports the comparison

between the different investigated probability distribution functions in the case of the PB9-L(12-82) and PB10-L(445-515) samples in terms of the probability density function, PDF, and cumulative distribution function, CDF, respectively. After preliminary considerations was carried out on sample PB9-L(12-82), the normal distribution function was discarded as not appropriate for representing the investigated entity. Therefore, its trend was not reported in Figure 5b, for sample PB10-L(445-515).

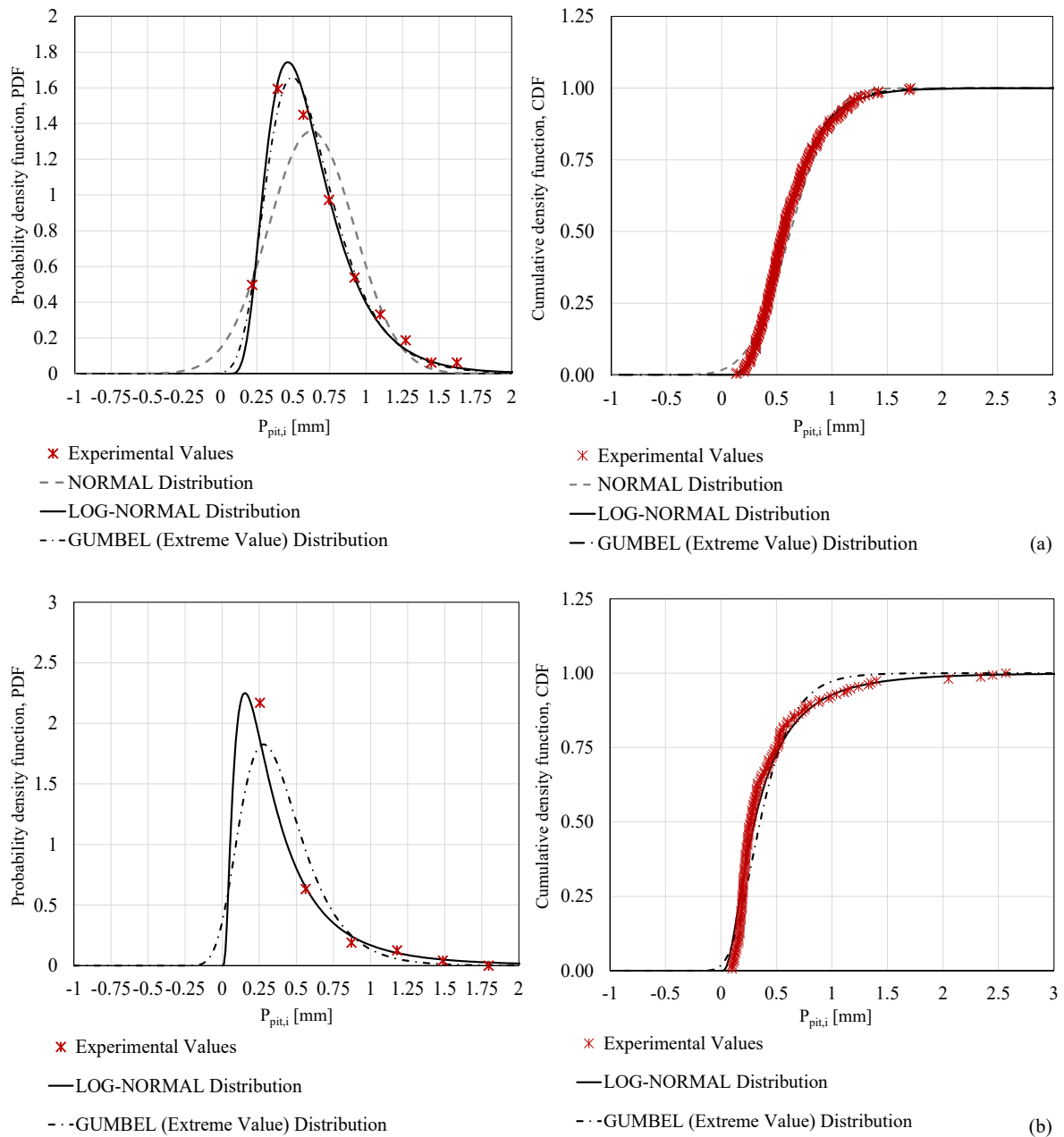


**Figure 5.** Comparison of adopted probabilistic distribution functions in terms of PDF and CDF for samples (a) PB9-L(12-82) and (b) PB10-L(445-515).

The outcomes show that the lognormal distribution function can be considered as the best-fitting distribution for the description of the spatial variability of penetration depth in corroded prestressing strands, as in Equation (6):

$$f_X(x) = \frac{1}{\sqrt{2\pi}\zeta_x x} \exp \left[ -\frac{1}{2} \left( \frac{\ln x - \lambda_x}{\zeta_x} \right)^2 \right] \quad (6)$$

where  $\lambda_x$  and  $\zeta_x$  are the mean value and the standard deviation of the adopted lognormal distribution function, respectively. In detail, the  $\lambda_x$  and  $\zeta_x$  values are reported in Table 2 for each sample analyzed.

**Table 2.** Key features of lognormal distributions of corroded prestressing strands.

Identifying Code	Mean Value $\mu_{pit}$ [mm]	Fractile 95% $P_{pit,0.95}$ [mm]	Max. Value $P_{pit,max}$ [mm]	$\lambda_x$	$\zeta_x$ [-]	$\alpha$ [-]
PB9-L(12-82)	0.570	1.180	1.710	-0.57	0.447	2.74
PB9-L(426-496)	0.165	0.465	0.424	-1.79	0.622	10.10
PB9-R(15-60)	0.611	1.431	2.784	-0.49	0.515	3.99
PB9-R(428-473)	-	-	-	-	-	-
PB10-L(138-208)	0.341	0.647	0.590	-1.08	0.391	10.84
PB10-L(445-515) *1	0.304	1.172	2.447	-1.20	0.824	6.09
PB10-R(287-332) *1	0.389	1.152	2.880	-0.94	0.659	5.72
PB10-R(32-102) *2	-	-	-	-	-	-
PB11-L(5-75)	-	-	-	-	-	-
PB11-L(196-266)	0.222	0.711	1.402	-1.51	0.709	6.28
PB11-R(6-51)	0.255	0.891	0.976	-1.36	0.760	8.02
PB11-R(273-318)	0.231	0.960	1.260	-1.47	0.867	5.27
PB12-L(12-82)	0.480	1.022	1.550	-0.73	0.459	2.90
PB12-L(124-169)	0.239	0.742	1.227	-1.43	0.693	4.00
PB12-R(100-170)	0.290	0.740	1.040	-1.24	0.572	3.23
PB12-R(358-403)	-	-	-	-	-	-
PB13-L(1-46)	0.380	0.900	1.460	-0.97	0.527	3.37
PB13-R(0-70)	0.450	0.924	1.380	-0.80	0.436	2.79
PB13-L(108-178) *1	0.486	1.471	1.840	-0.72	0.673	3.10
PB13-R(70-115)	0.240	0.810	1.090	-1.43	0.738	3.30
PB14-L(455-500)	-	-	-	-	-	-
PB14-L(10-55)	0.578	1.300	2.237	-0.55	0.491	3.42
PB14-R(2-72)	0.425	0.971	1.227	-0.86	0.505	2.53
PB14-R(77-122)	0.205	0.453	0.540	-1.60	0.488	3.24

\*1 Samples not considered in the following relationship because of outliers. \*2 Samples not considered because of 3D-scanning problems.

For the sake of completeness, the main outcomes of penetration depth obtained from the statistical analysis in terms of mean value,  $\mu_{pit}$ , fractile value at 95%,  $P_{pit,0.95}$ , and maximum value,  $P_{pit,max}$ , are also pointed out in Table 2.

Figure 6 shows the obtained results in terms of PDF and CDF for the different samples considered. It is evident how the samples characterized by limited corrosion deterioration show shallow or small-size pits generally widely spaced. On the other hand, with the increase of the level of corrosion, pits start to occur randomly along the sample length, having variable size and penetration depth, reaching over-sized dimension and a widespread diffusion for significant level of corrosion, as highlighted in Figure 6a.

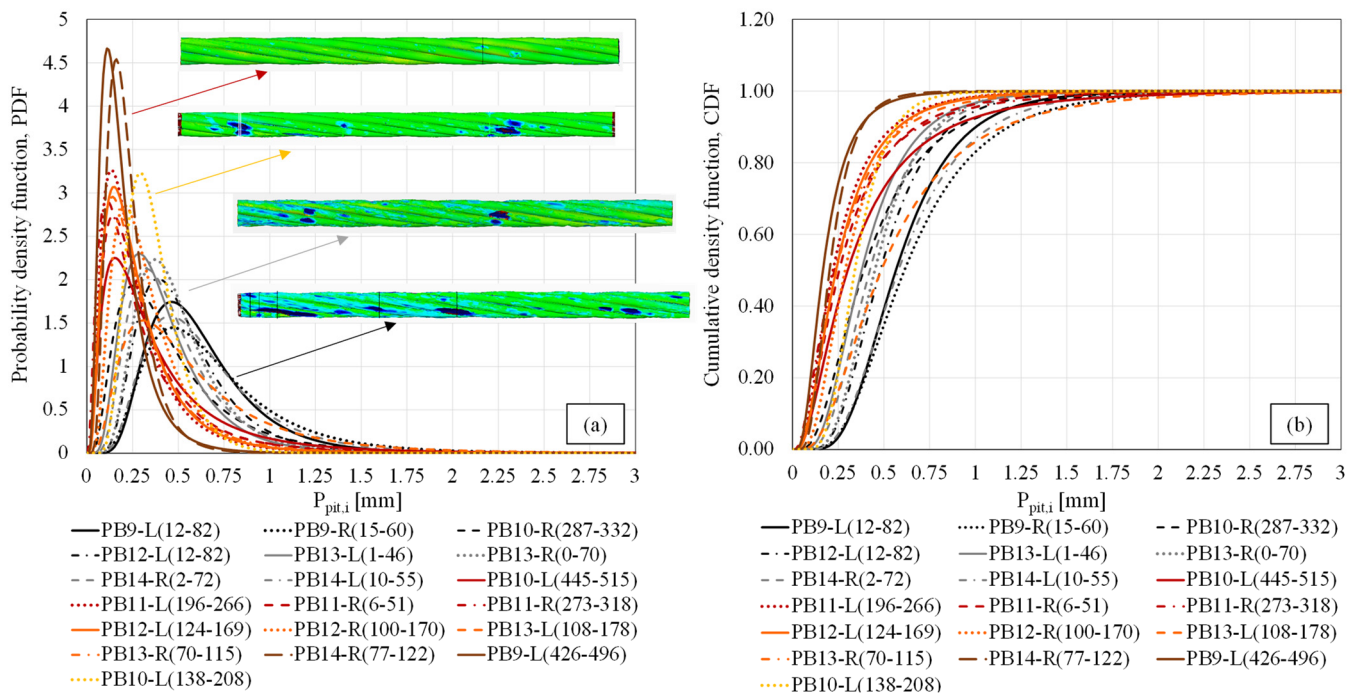


**Figure 6.** Probabilistic distribution functions of penetration depth of each corroded prestressing strand: (a) PDF and (b) CDF.

### 3.2. Pitting Factors Analysis

#### 3.2.1. Definition of Pitting Parameters

Referring to 3D-scanning outcomes, the maximum sectional penetration depth,  $P_{pit,max,sectional,i}$ , varies along the sample length.

In the present research, to completely characterize the pitting corrosion in both longitudinal and transversal directions, two pitting factors are calculated, named  $\alpha$  and  $\Omega_i$ , respectively. Both the pitting factors are indicators of the level of corrosion of prestressing strands and must be taken into consideration simultaneously for an exhaustive comprehension of pitting corrosion.

On one hand, the longitudinal pitting factor  $\alpha$  is unique for each corroded sample and describes the longitudinal (axial) condition of the corroded prestressing reinforcement. By definition,  $\alpha$  values are greater than or equal to 1.0 and are commonly evaluated as the ratio between the maximum penetration depth measured along the overall sample length,  $P_{pit,max}$ , and the average penetration depth calculated according to Equation (1),  $P_{pit,av,long}$ , as stated in Equation (7) and as shown in Figure 3.

$$\alpha = \frac{P_{pit,max}}{P_{pit,av,long}} \quad (7)$$

On the other hand, the transversal pitting factor  $\Omega_i$  is a sectional value calculated through the expression reported in Equation (8) and represents the relationship between the maximum penetration depth,  $P_{pit,max,sectional,i}$ , and the average penetration depth of external wires with the exception of the most corroded one,  $P_{pit,av,sectional,i}$ —previously evaluated by adopting Equation (2). According to the scanned length of each sample and

considering a sectional analysis every 10 mm (Figure 3), a total of 25 or 50 sectional values of the transversal pitting factor  $\Omega_i$  were measured, respectively.

$$\Omega_i = \gamma_i \cdot \beta_i = \frac{P_{pit,max,sectional,i}}{2r_{outer}} \frac{P_{pit,av,sectional,i}}{r_{outer}} = \frac{P_{pit,max,sectional,i}}{2r_{outer}} \frac{\frac{\sum_1^{n_{sectional}} P_{pit,sectional,i}}{n_{sectional}}}{r_{outer}} = \frac{\sum_1^{n_{sectional}} P_{pit,sectional,i}}{2r_{outer}} = \frac{\sum_1^{n_{sectional}} P_{pit,sectional,i}}{2r_{outer}} \tag{8}$$

The transversal pitting factor is obtained as the product between the intensity factor  $\gamma_i$  and the transversal factor  $\beta_i$  and it ranges between 0 and 1.0. In detail, the intensity factor  $\gamma_i$  is the coefficient representing the level of corrosion (intensity of corrosion) of the investigated section and is defined as the ratio between the maximum measured sectional penetration depth,  $P_{pit,max,sectional,i}$ , and two times the radius of the external uncorroded wire,  $r_{outer}$ . This latter ranges between 0 and 1.0, where 0 stands for the uncorroded scenario, whereas 1.0 stands for the critical scenario when the entire external wire is corroded. Besides, the transversal coefficient  $\beta_i$  reproduces the relationship that exists between the dimensionless average sectional penetration depth of the  $n_{sectional}$  external wires of the strand, except for the most corroded one,  $P_{pit,av,sectional,i}$ , with respect to the dimensionless maximum one,  $P_{pit,max,sectional,i}$ . The coefficient  $\beta_i$  ranges between 0 and 1.0, where 0 stands for the uncorroded scenario and 1.0 represents the scenario of homogeneous corrosion, meaning that the external prestressing wires are characterized in the transverse direction by the same penetration depth of the most corroded wire—regardless of the level of corrosion of the analyzed section.

### 3.2.2. Variation of Longitudinal Pitting Factor as a Function of Corrosion Level

The values of the longitudinal pitting factor  $\alpha$ , estimated by adopting the procedure described in the previous paragraph, are briefly reported in Table 2.

Figure 7 shows the variation of  $\alpha$  as a function of the dimensionless maximum penetration depth,  $P_{pit,max}$ . It is worth noting that, at this stage, the influence of surface defects is not considered, i.e., no distinctions between samples retrieved from areas of the tested PC beams showing the presence or the absence of longitudinal splitting cracks were considered.

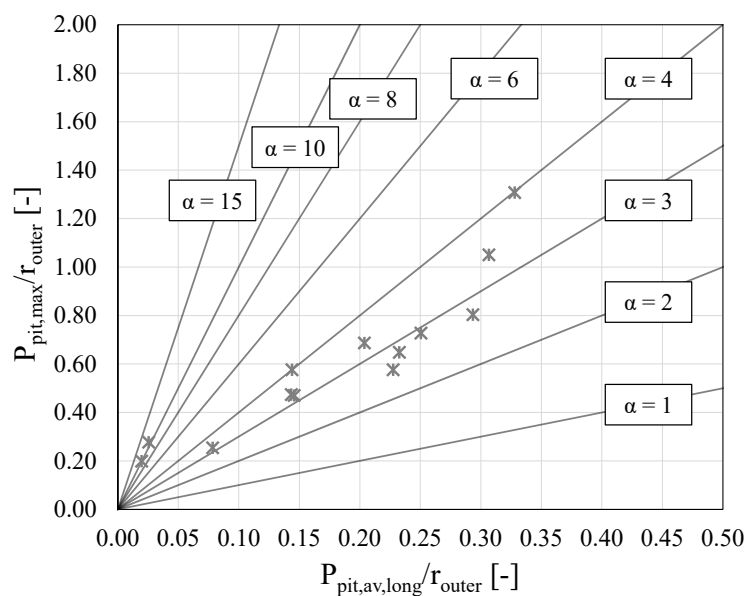


Figure 7. Variation of the longitudinal pitting factor  $\alpha$  as a function of  $P_{pit,max}$ .

As is visible from Figure 7, the longitudinal pitting factor  $\alpha$  is not constant but varies from sample to sample as a function of the longitudinal corrosion deterioration, expressed in terms of  $P_{pit,av,long}$  value. For a low value of the longitudinal average penetration depth,  $P_{pit,av,long}$ ,  $\alpha$  assumes values close to 10, which emphasizes a significant difference between the longitudinal maximum and average penetration depth. Conversely, when the level of corrosion increases, the gap between the longitudinal maximum and average penetration depth reduces, leading to lower values of the longitudinal pitting factor  $\alpha$ , which ranges between 4 and 2. In detail, the low  $\alpha$  values are closely related to a wider extent of the corrosion level along the length of the strand, meaning more diffuse pits with variable but significant penetration depths. Therefore, this yields a longitudinal corrosion level that is no longer localized but rather more homogeneous along sample length.

### 3.2.3. Sectional Correlation: Transversal Pitting Factor $\Omega_i$

Based on the several values of the transversal pitting factor  $\Omega_i$  measured from the sectional analysis of each corroded sample, a quadratic relationship of  $\Omega_i$  as a function of the dimensionless sectional maximum penetration depth,  $P_{pit,max,sectional,i}/r_{outer}$ , is proposed in Equation (9) and highlighted in Figure 8a:

$$\Omega_i = 0.189 \left( \frac{P_{pit,max,sectional,i}}{r_{outer}} \right)^2 + 0.125 \frac{P_{pit,max,sectional,i}}{r_{outer}} \quad (9)$$

where the upper boundary limit of  $P_{pit,max,sectional,i}/r_{outer}$  is set equal to 2.0—for a sectional maximum penetration depth equal to the diameter of uncorroded wire—meaning the total deterioration of the external wire. Then, the faithfulness of the proposed relationship is enhanced by the definition of the probabilistic confidence levels at 90% and 99%, which are drawn in Figure 8 with green and orange lines, respectively. For the sake of clarity, the confidence-level expressions at 90% and 99% are provided in Equations (10) and (11).

$$\Omega_i = 0.125 \frac{P_{pit,max,sectional,i}}{r_{outer}} + 0.189 \left( \frac{P_{pit,max,sectional,i}}{r_{outer}} \right)^2 \pm 1.86 \sqrt{0.00065 + 0.000132 \left( \frac{P_{pit,max,sectional,i}}{r_{outer}} \right)^2 - 0.000514 \left( \frac{P_{pit,max,sectional,i}}{r_{outer}} \right)^3 + 0.00057 \left( \frac{P_{pit,max,sectional,i}}{r_{outer}} \right)^4} \quad (10)$$

$$\Omega_i = 0.125 \frac{P_{pit,max,sectional,i}}{r_{outer}} + 0.189 \left( \frac{P_{pit,max,sectional,i}}{r_{outer}} \right)^2 \pm 2.76 \sqrt{0.00065 + 0.000132 \left( \frac{P_{pit,max,sectional,i}}{r_{outer}} \right)^2 - 0.000514 \left( \frac{P_{pit,max,sectional,i}}{r_{outer}} \right)^3 + 0.00057 \left( \frac{P_{pit,max,sectional,i}}{r_{outer}} \right)^4} \quad (11)$$

Moreover, to analyze the probabilistic distribution of  $\Omega_i$  measurements,  $\Omega_i$  values were first divided in function of  $P_{pit,max,sectional,i}/r_{outer}$  intervals with spacing equal to 0.05. Thereafter, similarly to the procedure adopted for the measured penetration depth along the corroded sample length, lognormal distribution functions were used to describe the variability of  $\Omega_i$  measurements in each interval. For the sake of completeness, the mean value,  $\lambda_l$ , and the standard deviation,  $\zeta_l$ , for each interval analyzed is reported in Table 3, whereas in Figure 8b are reported some lognormal distribution examples for selected  $P_{pit,max,sectional,i}/r_{outer}$  intervals. According to the latter, a noticeable dispersion of  $\Omega_i$  measurements is observed for  $P_{pit,max,sectional,i}/r_{outer}$  values higher than 0.2.

Finally, the fractile value of  $\Omega_i$  measurements at 95% was calculated for each  $P_{pit,max,sectional,i}/r_{outer}$  interval, as shown in Figure 8b and reported in Table 3. As a result, a polynomial interpolation function is proposed in Equation (12) to represent a realistic upper confidential boundary limit of  $\Omega_i$  measurements. It is worth noting that the proposed relationship is valid up to available experimental  $P_{pit,max,sectional,i}/r_{outer}$  values equal to 0.8.

$$\Omega_i = -1.1792 \left( \frac{P_{pit,max,sectional,i}}{r_{outer}} \right)^3 + 1.1019 \left( \frac{P_{pit,max,sectional,i}}{r_{outer}} \right)^2 + 0.178 \frac{P_{pit,max,sectional,i}}{r_{outer}} \quad (12)$$

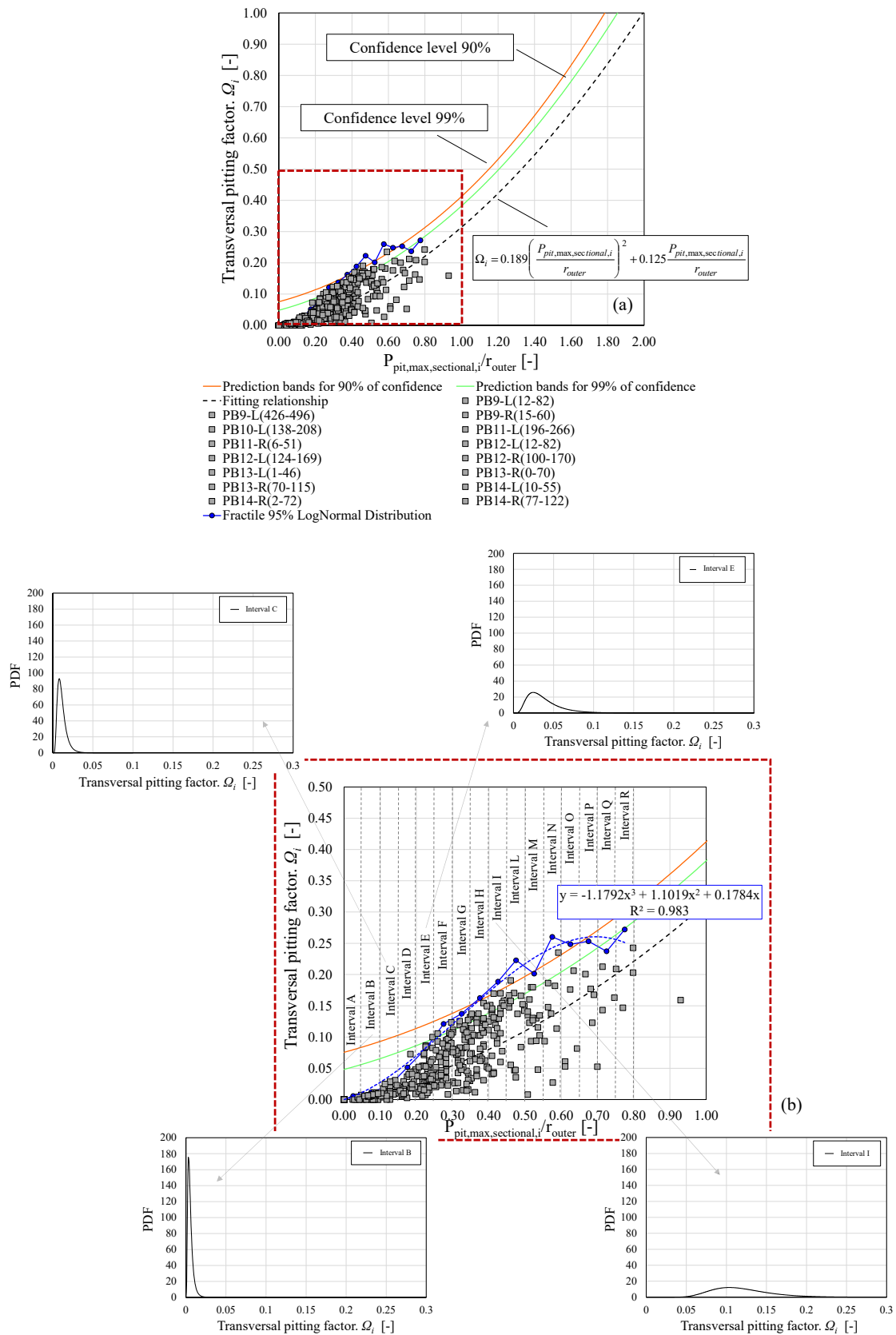


**Figure 8.** Transversal pitting factor  $\Omega_i$  vs. maximum sectional penetration depth,  $P_{pit,max,sectional,i}$ : (a) general expression and (b) variance of lognormal PDF for each interval of  $P_{pit,max,sectional,i}$ .

**Table 3.** Key features of lognormal distributions of  $\Omega_i$  measurements.

$P_{pit,max,sectional,i}/r_{outer}$ Intervals [-]	$\lambda_1$	$\zeta_1$ [-]	Fractile at 95% [-]
0.0–0.05	−7.169	1.214	0.0057
0.05–0.1	−5.382	0.580	0.0119
0.1–0.15	−4.601	0.484	0.0222
0.15–0.2	−4.012	0.636	0.0515
0.2–0.25	−3.412	0.546	0.0810
0.25–0.3	−2.820	0.431	0.1209
0.3–0.35	−2.705	0.440	0.1374
0.35–0.4	−2.433	0.375	0.1624
0.4–0.45	−2.176	0.309	0.1886
0.45–0.5	−2.136	0.386	0.2227
0.5–0.55	−2.194	0.360	0.2014
0.55–0.6	−2.057	0.434	0.2601
0.6–0.65	−2.316	0.562	0.2484
0.65–0.7	−2.013	0.390	0.2532
0.7–0.75	−1.776	0.205	0.2371
0.75–0.8	−1.627	0.196	0.2720

The powerfulness of the proposed correlations consists of the definition of a simplified approach for the sectional analysis of corroded strands that allows the prediction of the average penetration depth of corroded external wires,  $P_{pit,av,sectional,i}$ , by starting from the measurement of a single input parameter, that is, the maximum penetration depth of the analyzed section,  $P_{pit,max,sectional,i}$ . The flowchart of the simplified approach for the evaluation of the stress–strain relation of a corroded strand—starting from the measurement of the pit depth of the most corroded wire,  $P_{pit,max,sectional,i}$ —is reported in Figure 9. The simplified approach assumes the relationship between the transversal pitting factor  $\Omega_i$  and the dimensionless sectional maximum penetration depth  $P_{pit,max,sectional,i}/r_{outer}$  stated in Equation (9).

The relevance of the proposed approach enables to overcome the issue related to the estimation of the sectional average penetration depth of corroded wires during the in situ assessment of prestressing reinforcement. In fact, after the removal of the external concrete cover, in situ measurements such as the evaluation of the maximum penetration depth can exclusively involve the outward external wires only, without being able to significantly assess the condition of the remaining hidden wires. Vice versa, once the maximum penetration depth is known, the sectional average penetration depth can be predicted by adopting the relationships proposed in Equations (9)–(12) for different confidence levels (50%, 90%, 95% by considering experimental intervals of  $P_{pit,max,sectional,i}/r_{outer}$  or 99%).

In general, the following remarks can be drawn:

- At the initial stage—for  $P_{pit,max,sectional,i}/r_{outer}$  values up to 0.2—even if the sectional maximum penetration depth  $P_{pit,max,sectional,i}/r_{outer}$  can be locally significant, low values of the transversal pitting factor  $\Omega_i$  are predicted with negligible dispersion of measurement values, meaning that the remaining external wires are almost uncorroded.
- At the intermediate stage—for  $P_{pit,max,sectional,i}/r_{outer}$  values between 0.2 and 0.5—with the increase in the maximum penetration depth  $P_{pit,max,sectional,i}/r_{outer}$ , the values of the transversal pitting factor  $\Omega_i$  increase and show great dispersion of measurements, which means that the remaining external wires are affected by a variable corrosion deterioration at different sections.
- At the final stage—for  $P_{pit,max,sectional,i}/r_{outer}$  values between 0.5 and 0.8—since the corrosion deterioration tends to be more homogeneous sectionally and along the length of the corroded prestressing strands, the values of the transversal pitting factor  $\Omega_i$  have lower dispersion.
- Finally, the defined dimensionless average penetration depth,  $P_{pit,av,sectional,i}/r_{outer}$ , plays a fundamental role for the sectional prediction of the residual stress–strain response of

corroded prestressing strands when an equivalent spring approach is adopted, such as the one proposed by Franceschini et al. [19] and here summarized in Figure 9.

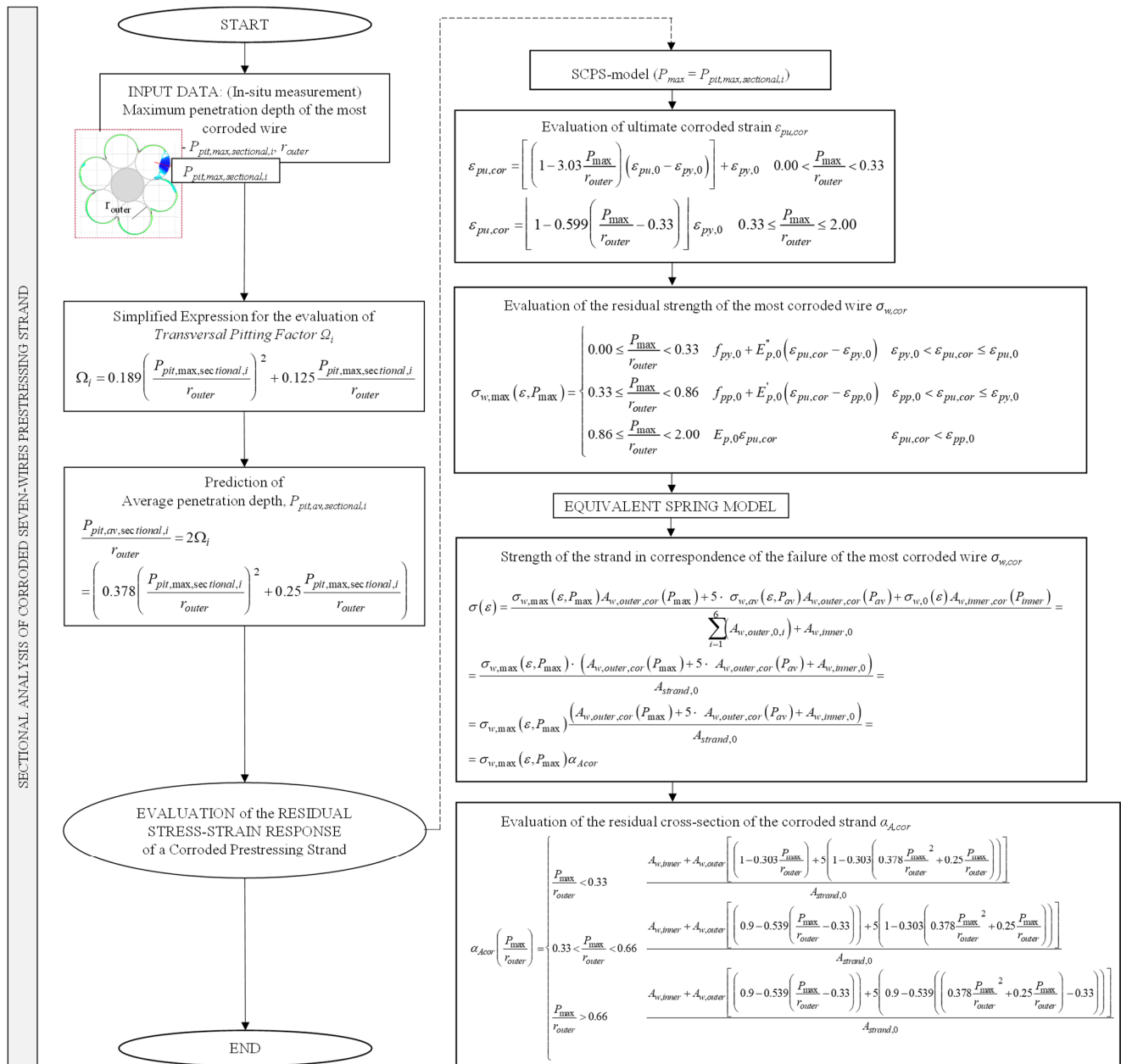


**Figure 9.** Flowchart of the proposed simplified approach, expressions for the prediction of residual stress-strain response coming from Franceschini et al. [19].

Based on the previous results, the expression for the evaluation of the dimensionless residual cross-section of the corroded strand,  $\alpha_{Acor}$  (Figure 9), can be modified to take into account the higher confidence levels of the relationship that correlates  $\Omega_i$  measurements and  $P_{pit,max,sectional,i}/r_{outer}$  values. The assumption of higher confidence levels—Equations (9)–(12)—leads to the estimation of a higher sectional average penetration depth,  $P_{pit,av,sectional,i}/r_{outer}$ , which results in a safer prediction of the ultimate strength,  $\sigma(\varepsilon)$ , as well as the ultimate tensile force of corroded prestressing strands. To this aim, Figure 10 highlights the trends of the dimensionless residual cross section parameter of the corroded strand,  $\alpha_{Acor}$ , for the different confidence levels taken into account.

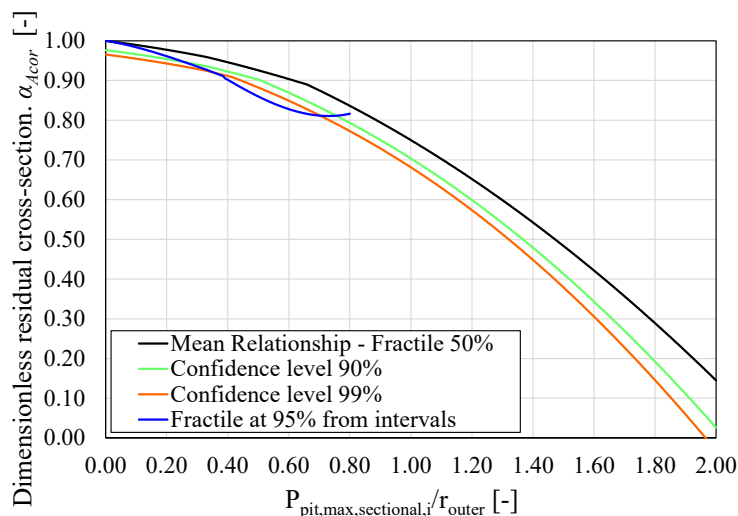


**Figure 10.** Different trend of the residual cross-section parameter  $\alpha_{Acor}$  for the different confidence levels of the relationship relating  $\Omega_i$  measurements and  $P_{pit,max,sectional,i}/r_{outer}$  values.

### 3.3. Discussion on Longitudinal Cracks Effect

Finally, to evaluate the measurement-based correlation that subsists between longitudinal splitting cracks and penetration depth, a correlation relating the maximum  $P_{pit,max}$  and the average penetration depths  $P_{pit,av,long}$  of corroded prestressing strands is proposed by taking into account the effects associated to surface defects induced by corrosion.

As a general remark, the level of corrosion of prestressing strands retrieved from zones of PC beams affected by longitudinal splitting cracks was higher than those from undamaged zones. The same outcomes were observed in the research carried out by Chen et al. [31] on 66 rebars extracted from plain concrete and fiber-reinforced concrete beams subjected to corrosion deterioration for more than 3 years. In particular, the pitting morphology of these samples exhibited deeper pits and a more homogeneous spatial variability of pitting with greater volume loss.

#### Correlation between Maximum and Average Penetration Depth

Referring to the data reported in Table 1 and considering the distinction between the corroded prestressing strands retrieved from cracked or uncracked areas of the investigated beams (Figure 1), a measurement-based correlation relating the maximum and longitudinal average penetration depths in their dimensionless form is introduced. As highlighted in Figure 11, the relationship can be discretized in three main phases, named uncracked phase, intermediate phase and cracked phase, the expressions of which are reported in Equations (13)–(15), respectively. The lower and upper boundary limits for the intermediate phase are fixed to best fit the experimental outcomes to a value of  $P_{pit,max}/r_{outer}$  equal to 0.50 and 0.60.

$$\text{Uncracked phase : } \frac{P_{pit,max}}{r_{outer}} = 5.56 \frac{P_{pit,av,long}}{r_{outer}} \tag{13}$$

$$\text{Intermediate phase : } \frac{P_{pit,max}}{r_{outer}} = 1.003 \frac{P_{pit,av,long}}{r_{outer}} + 0.411 \tag{14}$$

$$\text{Cracked phase : } \frac{P_{pit,max}}{r_{outer}} = 3.19 \frac{P_{pit,av,long}}{r_{outer}} \tag{15}$$

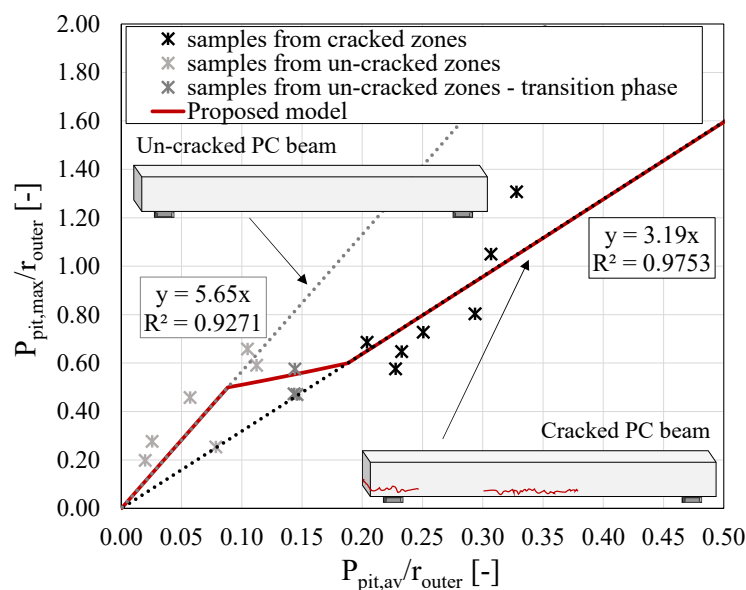


**Figure 11.** Correlation between dimensionless average and maximum penetration depth considering surface longitudinal cracks.

Generally, the proposed correlation shows the variation of the maximum penetration depth by considering or neglecting the influence of surface defects of concrete. In detail, the presence of longitudinal splitting cracks provides a preferential path for the penetration and diffusion of chloride ions into the concrete, leading to a higher level of corrosion of the prestressing reinforcement. Moreover, the presence of surface defects induces a more homogeneous spatial variability of corrosion with higher values of maximum and average penetration depths [32]. As a result, at the first stage, the diffusion of chloride ions toward the prestressing reinforcements is in general hindered by the presence of the uncracked concrete cover, except for the corroded samples coming from the beam-end sides characterized by the design deficiency. Therefore, for the remaining samples, the formation of localized and small pits is promoted at first, leading to high values of longitudinal pitting factor  $\alpha$  because of a big scatter between the maximum  $P_{pit,max}$  and the longitudinal average penetration depth  $P_{pit,av,long}$ . On the other hand, in the case of a cracked concrete cover, the homogenous spatial variability of corrosion is promoted, inducing lower differences between maximum and longitudinal average penetration depths, i.e., smaller pitting factors.

#### 4. Conclusions

The present study focused on the analysis of the pitting morphology of several naturally corroded prestressing strand samples. Toward this aim, a 3D-scanning technique and GOM Inspect software were adopted. Thereafter, a sectional analysis every 10 mm was carried out to measure the penetration depths of each external wire. Based on the measured data, several aspects have been investigated: (i) the distribution function of each corroded sample, (ii) the variation of longitudinal and transversal pitting factors, (iii) the correlations that subsist between the maximum and average penetration depth and (iv) the influence of longitudinal splitting cracks on the pitting corrosion of prestressing strands. The following conclusions can be drawn:

1. The lognormal distribution function is demonstrated to be the best distribution function for the fitting of penetration depth of corroded prestressing strands.
2. The outcomes reveal the need of simultaneously considering longitudinal and transversal pitting factors for the exhaustive comprehension of pitting corrosion. In detail, it is found out that with the increase in the level of corrosion a lower longitudinal pitting factor is obtained, meaning a more homogeneous spatial variability of pit-

ting corrosion for high levels of corrosion. In the present study,  $\alpha$  varies from 10 to approximately 2. On the other hand, based on the sectional calculation of the transversal pitting factor  $\Omega_i$ , a simplified approach for the prediction of the sectional average penetration depth  $P_{pit,av,sectional,i}$  of external wires as a function of the maximum one  $P_{pit,max,i}$  is proposed. In detail, different expressions are established to consider different confidential levels (90%, 95% by considering experimental intervals of  $P_{pit,max,sectional,i}/r_{outer}$  and 99%).

3. Based on the proposed correlations, a simplified approach for the sectional analysis of corroded strands that allows the prediction of the average penetration depth of corroded external wires,  $P_{pit,av,sectional,i}$ , by starting from the measurement of a single input parameter,  $P_{pit,max,sectional,i}$ , is defined. The approach overcomes the issue related to the estimation of the sectional average penetration depth of corroded wires during the in situ assessment of prestressing reinforcement. Then, the defined dimensionless average penetration depth,  $P_{pit,av,sectional,i}/r_{outer}$ , is assumed for the sectional prediction of the residual stress–strain response of corroded prestressing strands by adopting an equivalent spring model.
4. A correlation that relates the maximum  $P_{pit,max}$  and the longitudinal average penetration depths  $P_{pit,av,long}$  of corroded prestressing strands as a function of surface defects of concrete is presented. According to the latter, the presence of longitudinal splitting cracks provides a preferential path for the penetration and diffusion of chloride ions into the concrete, leading to a higher level of corrosion of prestressing reinforcement. As a result, the cracked phase shows a more homogenous spatial variability of corrosion leading to a lower difference between maximum  $P_{pit,max}$  and longitudinal average penetration depths  $P_{pit,av,long}$ .
5. Further studies will focus on a refined analysis of the variability of penetration depth from a probabilistic point of view by performing Monte Carlo analyses. Moreover, partial safety factors for corroded prestressing strands will be investigated.

**Author Contributions:** Conceptualization, L.F. and B.B.; methodology, L.F., B.B. and F.T.; software, L.F. and F.T.; validation, L.F. and J.S.; formal analysis, L.F.; investigation, F.T. and J.S.; resources, B.B.; data curation, L.F. and J.S.; writing—original draft preparation, L.F.; writing—review and editing, B.B., F.T. and J.S.; visualization, L.F.; supervision, B.B., F.T. and J.S.; project administration, B.B.; funding acquisition, B.B. All authors have read and agreed to the published version of the manuscript.

**Funding:** This research received no external funding.

**Informed Consent Statement:** Not applicable.

**Data Availability Statement:** The data that support the findings of this study are available from the corresponding authors upon reasonable request.

**Conflicts of Interest:** The authors declare no conflict of interest.

## References

1. Angst, U.M. Challenges and Opportunities in Corrosion of Steel in Concrete. *Mater. Struct. Constr.* **2018**, *51*, 4. [[CrossRef](#)]
2. Anania, L.; Badalà, A.; D’Agata, G. Damage and Collapse Mode of Existing Post Tensioned Precast Concrete Bridge: The Case of Petrulla Viaduct. *Eng. Struct.* **2018**, *162*, 226–244. [[CrossRef](#)]
3. West, J.S.; Larosche, C.J.; Koester, B.D.; Breen, J.E.; Kreger, M.E.; Substructures, P.B. *State-of-the-Art Report about Durability of Post-Tensioned Bridge Substructures*; University of Texas at Austin: Center for Transportation Research, TX, USA, 1999.
4. Woodward, R.J.; Williams, F. Collapse of Ynys-y-Gwas Bridge, West Glamorgan. *Proc. Inst. Civ. Eng.* **1988**, *84*, 635–669. [[CrossRef](#)]
5. Chen, W.; Xie, Y.; Guo, X.; Li, D. Experimental Investigation of Seismic Performance of a Hybrid Beam–Column Connection in a Precast Concrete Frame. *Buildings* **2022**, *12*, 801. [[CrossRef](#)]
6. United Nations Office for Disaster Risk Reduction. *GAR: Global Assessment Report on Disaster Risk Reduction*; United Nations Office for Disaster Risk Reduction: Geneva, Switzerland, 2019.
7. United Nations Office for Disaster Risk Reduction. *Making Critical Infrastructure Resilient: Ensuring Continuity of Service Policy and Regulations in Europe and Central Asia*; United Nations Office for Disaster Risk Reduction: Geneva, Switzerland, 2020.
8. Nürnberg, U. Corrosion Induced Failure Mechanisms of Prestressing Steel. *Mater. Corros.* **2002**, *53*, 591–601. [[CrossRef](#)]

9. Ahmad, S. Reinforcement Corrosion in Concrete Structures, Its Monitoring and Service Life Prediction—A Review. *Cem. Concr. Compos.* **2003**, *25*, 459–471. [[CrossRef](#)]
10. Akpanyung, K.V.; Loto, R.T. Pitting Corrosion Evaluation: A Review. *J. Phys. Conf. Ser.* **2019**, *1378*, 022088. [[CrossRef](#)]
11. Kioumars, M.; Benenato, A.; Ferracuti, B.; Imperatore, S. Residual Flexural Capacity of Corroded Prestressed Reinforced Concrete Beams. *Metals* **2021**, *11*, 442. [[CrossRef](#)]
12. El Menoufy, A.; Soudki, K. Flexural Behavior of Corroded Pretensioned Girders Repaired with CFRP Sheets. *PCI J.* **2014**, *59*, 129–143. [[CrossRef](#)]
13. Caines, S.; Khan, F.; Shirokoff, J. Analysis of Pitting Corrosion on Steel under Insulation in Marine Environments. *J. Loss Prev. Process Ind.* **2013**, *26*, 1466–1483. [[CrossRef](#)]
14. Darmawan, M.S.; Stewart, M.G. Effect of Pitting Corrosion on Capacity of Prestressing Wires. *Mag. Concr. Res.* **2007**, *59*, 131–139. [[CrossRef](#)]
15. Rinaldi, Z.; Imperatore, S.; Valente, C. Experimental Evaluation of the Flexural Behavior of Corroded P/C Beams. *Constr. Build. Mater.* **2010**, *24*, 2267–2278. [[CrossRef](#)]
16. Vecchi, F.; Franceschini, L.; Tondolo, F.; Belletti, B.; Sánchez Montero, J.; Minetola, P. Corrosion Morphology of Prestressing Steel Strands in Naturally Corroded PC Beams. *Constr. Build. Mater.* **2021**, *296*, 123720. [[CrossRef](#)]
17. Vereecken, E.; Botte, W.; Lombaert, G.; Caspeele, R. Assessment of Corroded Prestressed and Posttensioned Concrete Structures: A Review. *Struct. Concr.* **2021**, *22*, 2556–2580. [[CrossRef](#)]
18. Blomfors, M.; Larsson Ivanov, O.; Honfi, D.; Engen, M. Partial Safety Factors for the Anchorage Capacity of Corroded Reinforcement Bars in Concrete. *Eng. Struct.* **2019**, *181*, 579–588. [[CrossRef](#)]
19. Franceschini, L.; Belletti, B.; Tondolo, F.; Sanchez, J. A Simplified Stress-Strain Relationship for the Mechanical Behaviour of Corroded Prestressing Strands: The SCPS-Model. *Struct. Concr.* **2022**. [[CrossRef](#)]
20. Jeon, C.H.; Lee, J.B.; Lon, S.; Shim, C.S. Equivalent Material Model of Corroded Prestressing Steel Strand. *J. Mater. Res. Technol.* **2019**, *8*, 2450–2460. [[CrossRef](#)]
21. Belletti, B.; Rodríguez, J.; Andrade, C.; Franceschini, L.; Sánchez Montero, J.; Vecchi, F. Experimental Tests on Shear Capacity of Naturally Corroded Prestressed Beams. *Struct. Concr.* **2020**, *21*, 1777–1793. [[CrossRef](#)]
22. Vecchi, F.; Belletti, B.; Franceschini, L.; Andrade, C.; Rodriguez, J.; Montero, S.J. Flexural Tests on Prestressed Beams Exposed to Natural Chloride Action. In Proceedings of the CACRCS DAYS 2020, Online, 14 December 2020; pp. 205–212.
23. Belletti, B.; Stocchi, A.; Scolari, M.; Vecchi, F. Validation of the PARC\_CL 2.0 Crack Model for the Assessment of the Nonlinear Behaviour of RC Structures Subjected to Seismic Action: SMART 2013 Sharing Table Test Simulation. *Eng. Struct.* **2017**, *150*, 759–773. [[CrossRef](#)]
24. Li, D.; Wei, R.; Du, Y.; Guan, X.; Zhou, M. Measurement Methods of Geometrical Parameters and Amount of Corrosion of Steel Bar. *Constr. Build. Mater.* **2017**, *154*, 921–927. [[CrossRef](#)]
25. Tahershamsi, M.; Fernandez, I.; Lundgren, K.; Zandi, K. Investigating Correlations between Crack Width, Corrosion Level and Anchorage Capacity. *Struct. Infrastruct. Eng.* **2017**, *13*, 1294–1307. [[CrossRef](#)]
26. Franceschini, L.; Vecchi, F.; Tondolo, F.; Belletti, B.; Montero, S.J. Mechanical Behaviour of Corroded Strands under Chloride Attack: A New Constitutive Law. *Constr. Build. Mater.* **2022**, *316*, 125872. [[CrossRef](#)]
27. ASTM G1-03; Standard Practice for Preparing, Cleaning, and Evaluating Corrosion Test Specimens. ASTM: West Conshohocken, PA, USA, 2017.
28. Imperatore, S.; Rinaldi, Z.; Drago, C. Degradation Relationships for the Mechanical Properties of Corroded Steel Rebars. *Constr. Build. Mater.* **2017**, *148*, 219–230. [[CrossRef](#)]
29. Caprili, S.; Salvatore, W. Cyclic Behaviour of Uncorroded and Corroded Steel Reinforcing Bars. *Constr. Build. Mater.* **2015**, *76*, 168–186. [[CrossRef](#)]
30. Lu, C.; Yuan, S.; Cheng, P.; Liu, R. Mechanical Properties of Corroded Steel Bars in Pre-Cracked Concrete Suffering from Chloride Attack. *Constr. Build. Mater.* **2016**, *123*, 649–660. [[CrossRef](#)]
31. Chen, E.; Berrocal, C.G.; Löfgren, I.; Lundgren, K. Correlation between Concrete Cracks and Corrosion Characteristics of Steel Reinforcement in Pre-Cracked Plain and Fibre-Reinforced Concrete Beams. *Mater. Struct. Constr.* **2020**, *53*, 33. [[CrossRef](#)]
32. Franceschini, L.; Belletti, B.; Sanchez, J.; Tondolo, F. Dependency of Pitting Corrosion Spatial Variability on Crack Pattern of Prestressed Concrete Members. In Proceedings of the 14th fib PhD Symposium, Rome, Italy, 5–7 September 2022.